Grain size effect on tensile properties and slip systems of pure magnesium

Kang Wei [a,†], Rong Hu [b,†], Dongdi Yin [c], Lirong Xiao [a], Song Pang [d], Yang Cao [a], Hao Zhou [a,*], Yonghao Zhao [a,*], Yuntian Zhu [a,e,*]

[a] Nano and Heterogeneous Materials Center, School of Materials Science and Engineering, Nanjing University of Science and Technology, Nanjing 210094, China
[b] Herbert Gleiter Institute of Nanoscience, School of Materials Science and Engineering, Nanjing University of Science and Technology, Nanjing 210094, China
[c] Key Laboratory of Advanced Technologies of Materials, Ministry of Education, School of Materials Science and Engineering, Southwest Jiaotong University, Chengdu 610031, China
[d] Shanghai Metal Materials Near-Net-Shape Engineering Research Center, Shanghai Spaceflight Precision Machinery Institute, Shanghai 201600, China
[e] Department of Materials Science and Engineering, City University of Hong Kong, Hong Kong 999077, China

ARTICLE INFO

ABSTRACT

Grain refinement can significantly enhance the strength of metallic materials, but usually at the sacrifice of ductility. Here we report that refinement of magnesium grains can not only improve its strength, but also its ductility, due to the activation of more slip systems. It is found that pure Mg with coarse grain size ($\bar{d}$=125 μm) has a low ductility and uniform elongation (5.3%), due to the limited basal slip systems. In contrast, fine-grained Mg ($\bar{d}$=5.5 μm) exhibits enhanced work hardening and ductility as well as uniform elongation (18.3%). Two beam condition TEM analysis revealed that the improved properties were due to the activation of non-basal dislocations, such as $<c>$ and $<c + a>$ dislocations with reducing the grain sizes. It is also found that the $<c + a>$ dislocations are unstable and can dissociate into either $<c>$ and $<a>$ dislocations or I1 stacking faults. Contributions of nano stacking faults on strengthening and ductilization as well as their formation mechanism are rationalized and discussed.

© 2021 Acta Materialia Inc. Published by Elsevier Ltd. All rights reserved.

1. Introduction

Due to increasing energy crisis and greenhouse effect, lightweight alloys, such as magnesium alloys, are attracting more attentions for potential applications in aerospace, transportation and biomedical industries [1]. In general, Mg alloys can be further strengthened via solution and precipitation hardening, but often at the expense of ductility [2]. Because of its hexagonal close-packed (HCP) structure, Mg has only two independent easy slip systems (basal (0001) $<11\bar{2}0>$) at room temperature, which is insufficient for continuous deformation without cracking according to the Von Mises criterion [3]. Consequently, novel strategies to introduce additional deformation modes, such as non-basal slipping and twinning, have attracted increasing attention in the past decade [4,5].

Careful inspection of literature revealed that the additional slip systems in Mg can be activated by two different approaches: el-

evating deformation temperature and alloying with rare earth elements. It has been reported that non-basal slip systems such as prismatic and pyramidal slips can be activated by increasing the deformation temperature, which improves the formability of Mg [6,7]. When the deformation temperature is increased to more than 300 °C, the difference in the activation energies of basal and non-basal slips is reduced substantially [8], which makes it possible for magnesium alloys to be deformed to high strains, even to the severe plastic deformation regime [9,10]. This approach of introducing more non-basal slip systems at high temperatures has been widely used in industrial deformation of Mg alloys.

The alloying approach to activate more slip systems has been intensively studied and reported in literature. First principle calculations predicted that many potential elements, including rare earth (Y, Gd, and Nd), Ca, and Sn, promote non-basal slips [11]. Among them, Y and Ca are considered the most promising alloying elements, because they can reduce both the stacking fault energy [12] and the energy barrier of cross slip [13]. These predictions have been verified by experimental observations, in which high density of non-basal dislocations are found in binary Mg-Y and Mg-Ca alloys [14,15]. Basically, the physical mechanism for the

activation of non-basal slip systems is believed as distortion of local lattice and rearrangement of electronic charges caused by alloying elements [16,17].

Recent studies on metallic nano-materials have revealed grain size effect on deformation mechanisms. Zhu et al. [18,19] reported that twinning in face-centered cubic (fcc) metals is significantly affected by grain size. It is found that twinning in coarse grained metals is impeded by grain refinement, whereas an optimum grain size for twinning exists in nanocrystalline metals [20]. Cheng et al. [21] found that the volume fraction of edge, screw and mixed dislocations in body-centered cubic (bcc) Mo changed systematically with decreasing grain size in ultrafine-grained and nanostructured samples. In HCP structural Mg alloys, effect of grain size on mechanism of plastic deformation has also been reported [22–26]. According to the simulation of discrete dislocation dynamic on pure Mg, a transition of deformation mechanism from twinning to dislocation slip occurs when Mg grains are reduced to 2.7 μm [27]. Zeng et al. [28] found ultra-high plasticity in rolled pure Mg with a fine grain size of ~1.3 μm. The dominant deformation mechanism may change to intergranular slip in fine grained pure Mg, when the strain rate is reduced to less than 1×10^{-5} s^{-1} [29–31]. Liu et al. [5] observed a real time $\langle c + a \rangle$ dislocation slip in pure Mg nano-pillars with a size of ~400 nm. They believed that small crystal size led to high flow stress, which in turn activated $\langle c + a \rangle$ dislocations to accommodate plasticity. However, it is still unclear how the grain size affects deformation mechanisms in pure Mg, especially the non-basal slips, owing to the lack of systematic experimental investigation.

In this work, three pure Mg samples with different grain sizes ranging from 125 to 5.5 μm were studied primarily using transmission electron microscopy (TEM) in order to uncover the grain size effect on deformation mechanisms. It is found that non-basal dislocations including $\langle c \rangle$ and $\langle c + a \rangle$ dislocations were activated as the grain size was decreased to less than 50 μm. High flow stress in fine-grained sample is believed as the reason for the activation of non-basal slips. Based on in-depth analysis on the structure of stacking faults, contributions of nano stacking faults on strengthening and ductilization as well as their formation mechanism are rationalized. In addition, we also reveal that $\langle c + a \rangle$ dislocations are unstable and have two different ways of dissociation to form either $\langle c \rangle$ and $\langle a \rangle$ dislocations or I1 stacking faults in the grain interior.

2. Experimental procedures

A commercial pure Mg plate was punched into ϕ10 mm disks and thinned to ~2 mm for high pressure torsion (HPT) processing, which was performed at room temperature under 1 GPa for 10 revolutions at 1.5 rpm to refine its grains [32]. The HPT-processed samples were annealed at 450 °C, 350 °C, and 280 °C for 1 h to obtain different grain sizes. Note that, the critical temperature of recrystallization and recovery of pure Mg is higher than some of Mg alloy [33]. For the deformation defects, i.e. dislocations, to completely recover, the annealing temperature of pure magnesium should be higher than 250 °C. Previous works revealed that the work hardening capability of the samples annealed below 200 °C is poor, which resulted in lower ductility than that of coarse-grained samples [34,35]. Uniaxial tensile tests were performed at a strain rate of 2×10^{-3} s^{-1} using dog-bone shaped samples with a gage length of 4 mm and a transverse section of 1×1 mm^2 to investigate the grain size effect on mechanical properties. To ensure repeatability and accuracy of testing, at least 3 specimens in each condition were performed. Additionally, the elastic distortion induced by testing apparatus was corrected by equating the elastic portion of the whole curves to the theoretical elastic modulus of magnesium (43 GPa). Scanning electron microscopy (SEM)

observation was performed on a FEI Quanta 250F to observe fracture surfaces of the pure Mg samples after tensile loading. Electron back scattering diffraction (EBSD) were carried out in a Zeiss Auriga field-emission SEM equipped with an Oxford electron beam backscatter diffraction detector. The observation direction of EBSD is perpendicular to the plane of HPT disk. To understand the microstructural evolution at the sample surface, tensile testing was interrupted at desired strain, and areas in the gage center of the specimen was investigated using EBSD. The step size was chosen as one tenth of the grain size. The average EBSD indexing rate was above 0.85 in all the samples. Samples for EBSD experiment were ground with sandpapers of 320, 800, 1200 and 2000 grits, followed by a mechanical polishing to a mirror finish surface. Electropolishing was performed in an ethanol solution with 4% of perchloric acid at 30 V and −30 °C for 150 s before EBSD characterization.

Cross-sectional TEM specimens were cut from the tensile-deformed samples and gently polished to a thickness of ~25 μm. Perforation was conducted on a Gatan PIPS 691 ion milling machine with a low energy (4 KeV) and a low angle (3.5°). TEM observation was carried out by an aberration-corrected high-resolution transmission electron microscope (FEI Titan G2 60–300) operated at 300 kV. Digital Micrograph plug-in was used for geometric phase analysis (GPA).

3. Results and analysis

3.1. Microstructures of HPT-processed and annealed pure Mg samples

The starting materials are ultra-fine pure Mg (99.9%) processed by HPT, which has an average grain size ($\bar{d}$) of ~273 nm (Fig. 1). Annealing at different temperatures of 450 °C, 350 °C, and 280 °C for 1 hour produced recrystallized grain with average sizes of 125, 51 and 5.5 μm, respectively (Fig. 2a-2, b-2 and c-2). Mechanical behavior, such as Hall-Petch relationships and tension-compression asymmetry in Mg alloys, is affected by the texture, owing to their hexagonal close-packed crystal structure [36–38]. Inverse pole figure (IPF) mapping of EBSD images indicates that all of the annealed samples have a weak and random basal texture as well as a low fraction of low angle grain boundaries (LAGBs, 2–15°), as shown in Fig. 2a-3, b-3 and c-3. Materials with weak texture are adequate for studying the grain size effect on tensile properties and deformation mechanism.

3.2. Tensile properties and fracture surfaces

Fig. 3a shows the tensile stress-strain curves of pure Mg samples with different grain sizes. Yield strength (YS) and ultimate tensile strength (UTS) of the coarse-grained sample ($\bar{d}$=125 μm) are only 67.7 MPa and 137.6 MPa, respectively. The uniform elongation ε_{ue} and elongation to failure ε_{ef} of the annealed coarse-grained Mg sample are 5.3% and 6.3%, respectively. As the grain size is decreased to 51 μm and 5.5 μm, the YS is increased to 74.2 MPa and 93.8 MPa, respectively, and the UTS is enhanced to 165.6 MPa and 199.5 MPa, respectively. Most importantly, different from the conventional strength-ductility trade-off paradox, the ductility is not decreased, but significantly increased with the reduction of grain size (Fig. 3b).

Fig. 3c illustrates that the strain hardening rate ($\Theta = \partial\sigma/\partial\varepsilon$, σ is true stress, and ε is true strain) drops at first for all of the three samples with strain. Importantly, the true strain is larger than 4%, the samples with smaller grain size shows slower Θ drop with increasing strain. In other words, samples with smaller grains exhibited higher strain hardening rate, which is very unusual. This is also reflected in the strain hardening exponent n, [39], which increased with decreasing grain size: 0.32 (125 μm), 0.35 (51 μm) and 0.39 (5.5 μm). Based on Hart's theory [40], during tension
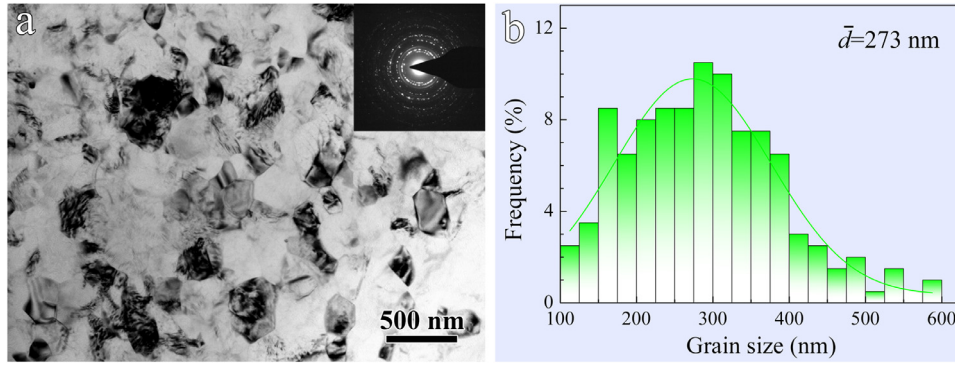
Fig. 1. Microstructure of pure Mg processed by HPT: (a) bright field TEM image and (b) corresponding grain size distribution.
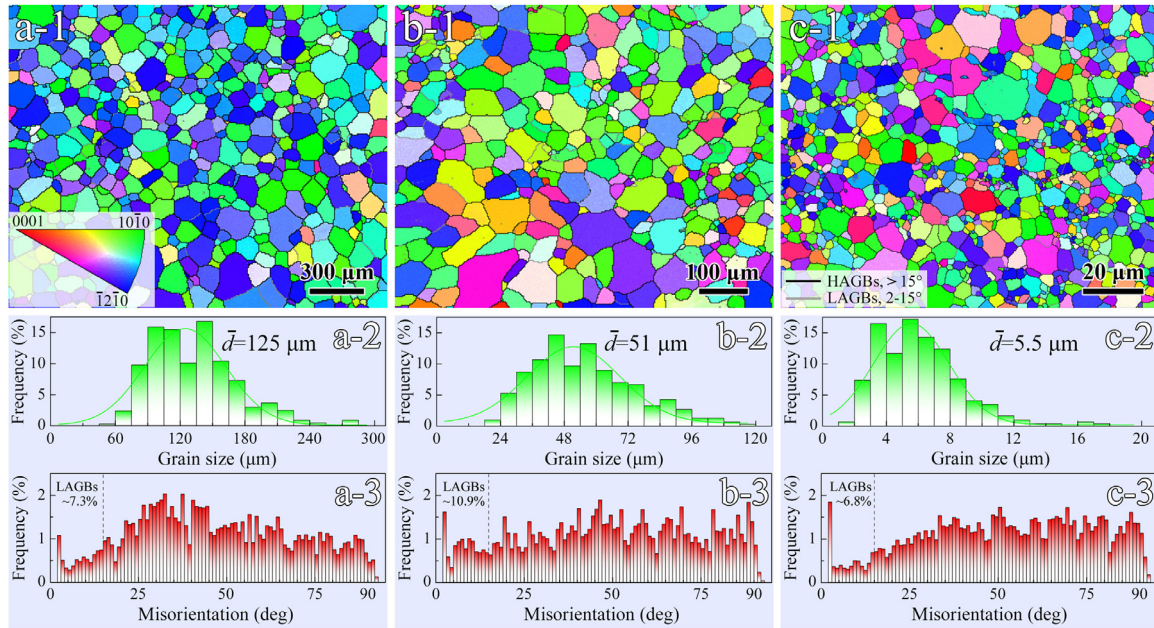

Fig. 2. EBSD micrographs of post annealed pure Mg: (a-1) to (c-1) inverse pole figure (IPF) mappings, (a-2) to (c-2) grain size distributions, (a-3) to (c-3) misorientation angle distributions of the samples annealed at 450 °C, 350 °C and 280 °C, respectively.

necking instability occurs when:

$$\Theta \leq \sigma\,(1-m) \tag{1}$$

where m is strain rate sensitivity. The strain hardening rate Θ is mainly resulted from dislocation accumulation. Both high Θ and m are important for high tensile ductility because they can help delay necking and consequently prolong uniform elongation. In this work, we performed tensile test with a strain rate of $2 \times 10^{-3}\ s^{-1}$. The average grain sizes of all the samples used in this case are larger than 5 μm. According to the tensile jump tests performed by Figueiredo et al. [30] and Zheng et al. [41], the value of m is estimated as ~0.03. Therefore, Eq. (1) can be approximated as:

$$\Theta \leq \sigma \tag{2}$$

which becomes the Considère criterion for necking initiation.

As shown in Fig. 3c, the dramatic drop of Θ in coarse-grained Mg caused necking onset at low strain. While the slow drop of Θ in fine-grained Mg delayed the necking occurrence and improved ductility. In literature, the slow drop of Θ and large n are usually caused by additional deformation mechanism, for example, twinning or phase transformation in TRIP and TWIP steels [42], or further dislocation accumulation by complex stresses in gradient materials [43]. We will probe the dislocation origin of large n and Θ for fine-grained Mg in following sections.

Fig. 3d, e, and f show the fracture surface of the samples with different grain sizes. The fracture surface of coarse-grained pure Mg is dominated by cleavage facets and tearing ridges, indicating a brittle-like fracture during tensile deformation (Fig. 3d-2). In contrast, a large number of small and shallow dimples are observed in the fracture surface of medium and fine-grained Mg (Fig. 3e-2 and f-2). These observations indicate that grain refinement led to higher plasticity and toughness fracture in pure Mg.

3.3. Deformed structures of the annealed Mg samples at 2.5% tensile strain

To reveal deformation mechanisms of the Mg samples, we performed rigorous EBSD and TEM analyses on the tensile specimens deformed to different strains. Fig. 4a-1, b-1 and c-1 show the inverse pole figures (IPFs) of the samples subjected to a tensile strain of 2.5%, in which high angle grain boundaries (HAGBs, >15 °) and low angle GBs (LAGBs) (2–15 °) are marked by black and gray lines, respectively. Clearly, no recrystallization or grain refinement occurred when the samples are deformed to such a low strain at room temperature. However, the fractions of LAGBs are significantly increased from 7.3%, 10.9% and 6.8% (Fig. 2a-3, b-3 and c-3) to 53.8%, 37.6% and 36.4% (Fig. 4a-3, b-3 and c-3), respectively. It is widely accepted that formation of LAGB in Mg alloys is re-
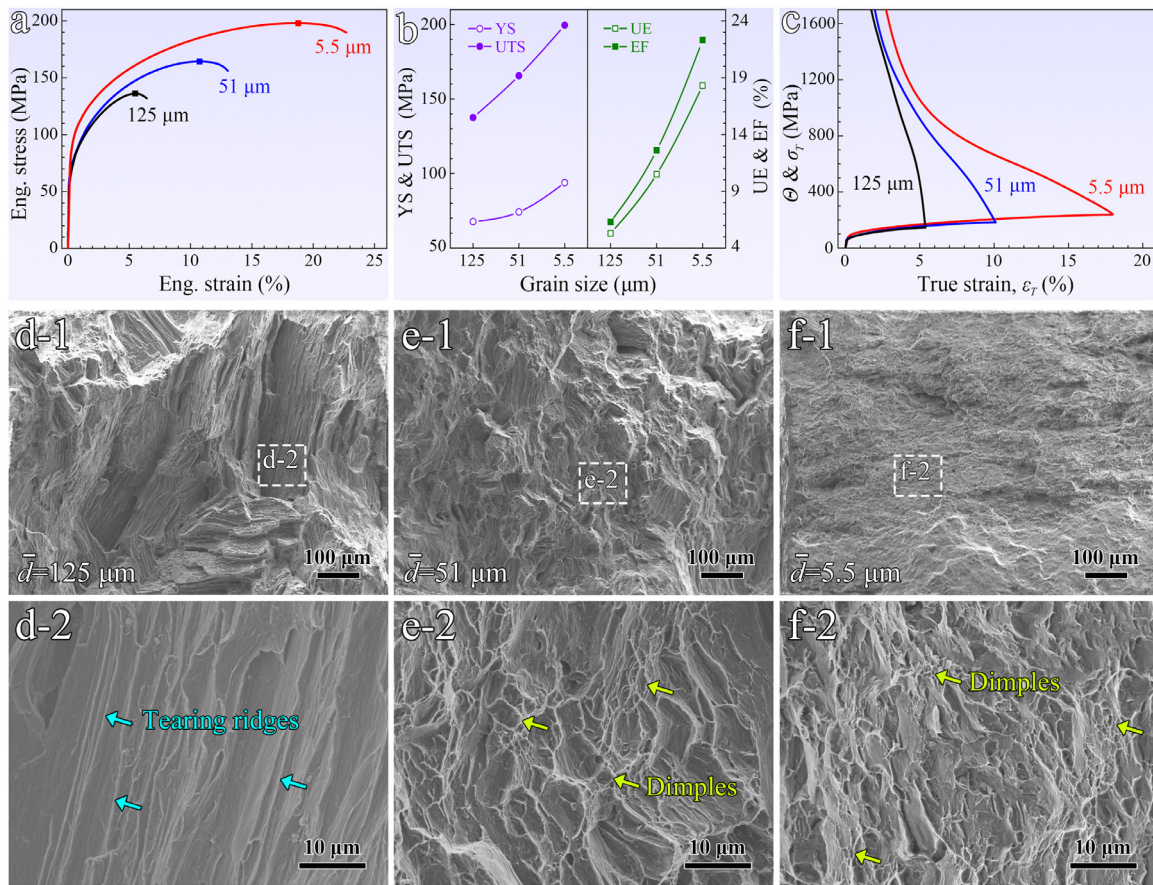
Fig. 3. Mechanical properties and fractography of pure Mg with different grain sizes: (a) uniaxial tensile engineering strain-stress curves, (b) yield strength (YS), ultimate tensile strength (UTS), uniform elongation ε_{ue}, and elongation to failure ε_{ef} of the samples with different grain size, (c) true stress (σ_{true}) and strain hardening (Θ) curves from tensile tests, (d-1), (e-1) and (f-1) SEM micrographs of fracture surfaces of the pure Mg with grain sizes of 125 μm, 51 μm and 5.5 μm, (d-2), (e-2) and (f-2) close-up images of (d-1), (e-1) and (f-1).

lated to the pile-up of geometrically necessary dislocations [44]. Larger grain size led to more LAGBs formed in pure Mg under a same deformation strain, which reveals that configuration and slipping of dislocations are affected by grain size. Fig. 4a-2, b-2 and c-2 show the Kernel average misorientation (KAM) images in the same areas. Clearly, larger KAM values are located mainly near the GBs in all samples. Dislocations in coarse-grained Mg are easier to entangle, forming high density dislocation walls and LAGBs. In all the three tensile deformed samples, a particular lamellar structure is found (marked by red arrows), which has a typical misorientation of $\{10\bar{1}2\}$ tensile twin (~86 °), as shown in Fig. 4a-3, b-3 and c-3. Brown et al. [45] reported that deformation twinning is active in magnesium when loaded in compression transverse to the basal poles. Twinning mechanism results in a characteristic finite reorientation of the crystal to a preferential direction for $\langle c + a \rangle$ slipping.

Fig. 5a shows a bright field TEM image of $\{10\bar{1}2\}$ deformation twin in pure Mg (5.5 μm), which is identified by the inset selected area diffraction pattern. The twin has a thickness of ~360 nm, and a high density of nano stacking faults with average spacing of ~55 nm are visible in the twin lamellae (Fig. 5b). There are theoretically at least seven twinning modes in hcp metal, including $\{10\bar{1}1\}$, $\{10\bar{1}2\}$, $\{10\bar{1}3\}$, $\{11\bar{2}1\}$, $\{11\bar{2}2\}$, $\{11\bar{2}3\}$ and $\{11\bar{2}4\}$ [46]. Among them, $\{10\bar{1}2\}$ twin is frequently observed in grains with c-axes are in tension [47]. Additionally, high densities of nano stacking faults have been demonstrated to improve strength efficiently, while maintaining good ductility in Mg [48]. As shown in Fig. 5c, the neighboring crystal structures are mirror symmetrical along twin boundary, sharing the same [1$\bar{2}$10] zone axis. It

is found that a stacking fault is growing from the twin boundary by a slipping partial dislocation. According to Hall-Petch relationship [49] and strengthening model of parallel stacking faults [50], the room temperature yield strength, $\sigma_{0.2}$, increased linearly with the reciprocal of square root of grain size and average spacing of stacking faults, respectively.

3.4. Dislocation configurations in deformed Mg samples

To identify the active slip systems in deformed pure Mg samples, two-beam conditions were set during TEM observations according to the invisibility criterion of $\boldsymbol{g} \cdot \boldsymbol{b} = 0$, where $\boldsymbol{g}$ and $\boldsymbol{b}$ represent the reflection and Burgers vector, respectively. If a particular reflection is set as $\boldsymbol{g} = 0002$, $\langle c \rangle$ dislocations with $\boldsymbol{b} = \langle 0001 \rangle$ are viewed edge on, while $\langle a \rangle$ dislocations with $\boldsymbol{b} = 1/3\langle 11\bar{2}0 \rangle$ are invisible in bright field TEM images. In contrast, when the two-beam situations are set as $\boldsymbol{g} = 0\bar{1}10$ or $\boldsymbol{g} = 2\bar{1}\bar{1}0$, $\langle a \rangle$ dislocations become visible, while $\langle c \rangle$ dislocations are invisible. Additionally, $\langle c + a \rangle$ dislocations with $\boldsymbol{b} = 1/3\langle 11\bar{2}3 \rangle$ are visible in all above-mentioned two-beam conditions [51,52]. Therefore, the type of dislocations can be determined by comparative analyzing of images in the same region obtained from different two-beam conditions. Due to the limited observation area in TEM, we observed at least 30 grains in each sample to obtain meaningful statistics. Grain boundaries and perforation edges are included in images to mark the exact position of observation.

Fig. 6 shows dislocation configurations in the coarse-grained Mg ($\bar{d}$=125 μm) deformed to 2.5% and 5% strain, respectively. Compared with bright field images in two-beam conditions of $\boldsymbol{g} = 0\bar{1}10$
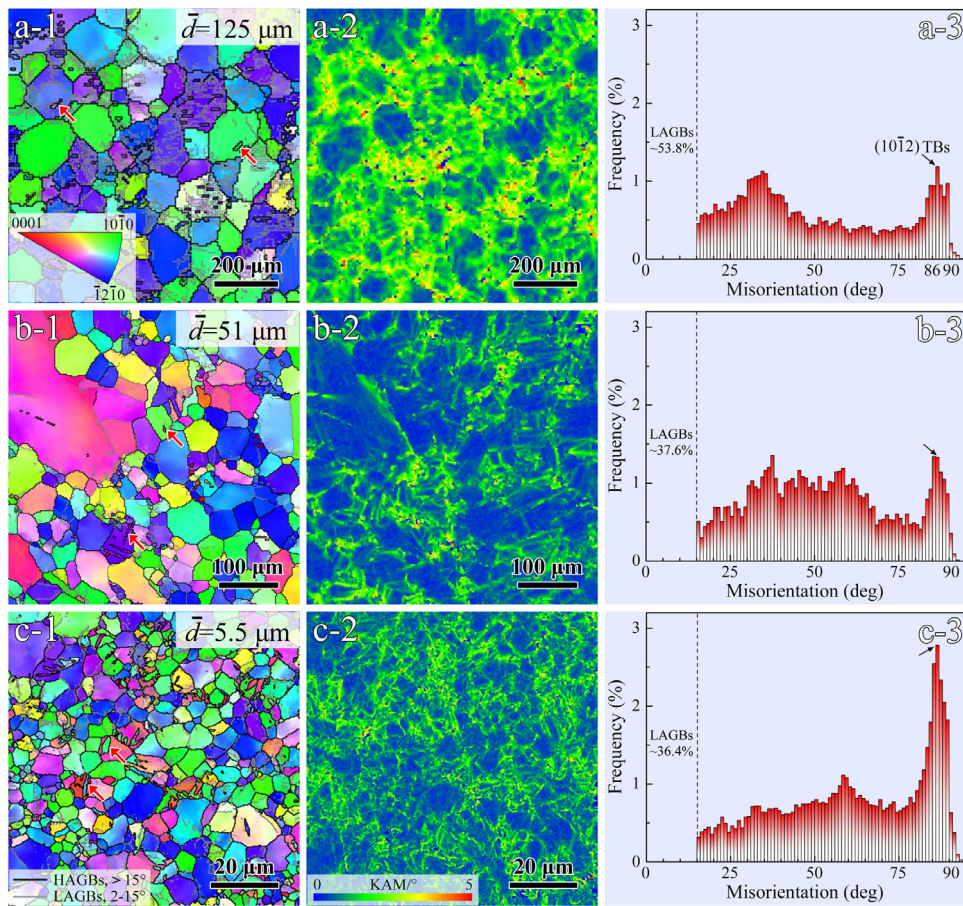
Fig. 4. EBSD images of 2.5% tensile deformed pure Mg samples: (a-1) to (c-1) IPF mappings, (a-2) to (c-2) KAM mappings, (a-3) to (c-3) misorientation angle distributions with grain sizes of 125, 51 and 5.5 μm, respectively.
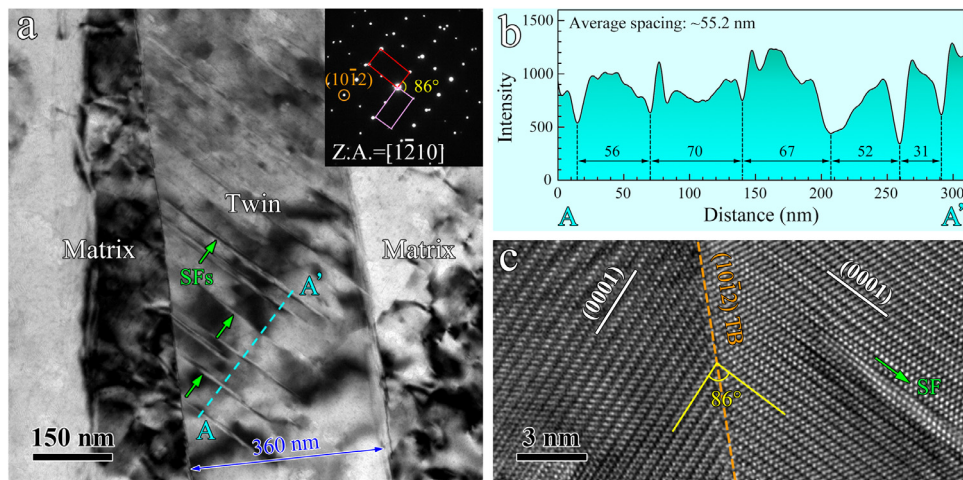

Fig. 5. TEM images of {10$\bar{1}$2} deformation twin in pure Mg (5.5 μm): (a) bright field image inserted with selected area diffraction pattern, (b) intensity of stacking faults contrast in (a), (c) high resolution TEM image in [1$\bar{2}$10] zone axis.

(Fig. 6a-1) and g = 0002 (Fig. 6a-2), all dislocations are invisible in the two-beam situation of g = 0002, indicating only basal $\langle a \rangle$ dislocations, marked by the yellow arrows, were formed in the deformed sample. It has been well established that basal slip systems are much easier to be activated in HCP metals, owing to their low critical resolved shear stress (CRSS) [53]. Fig. 6b-1 and b-2 show a set of bright field images of the sample deformed to failure (~5% strain) in the same two-beam conditions. With increas-

ing deformation strain, the dislocation density is increased from 4.2×10^{12} m^{-2} to 1.4×10^{13} m^{-2} (Fig. 6c). However, the type of dislocation does not change and is still dominated by basal $\langle a \rangle$ dislocations during straining.

Fig. 7 shows dislocation configurations in a Mg with an average grain size of 51 μm at tensile strains of 2.5% and 9.5%. A high density of basal $\langle a \rangle$ dislocations are observed in (0001) planes when the reflection is set as g = 0$\bar{1}$10 (Fig. 7a-1 and b-1). In addition,
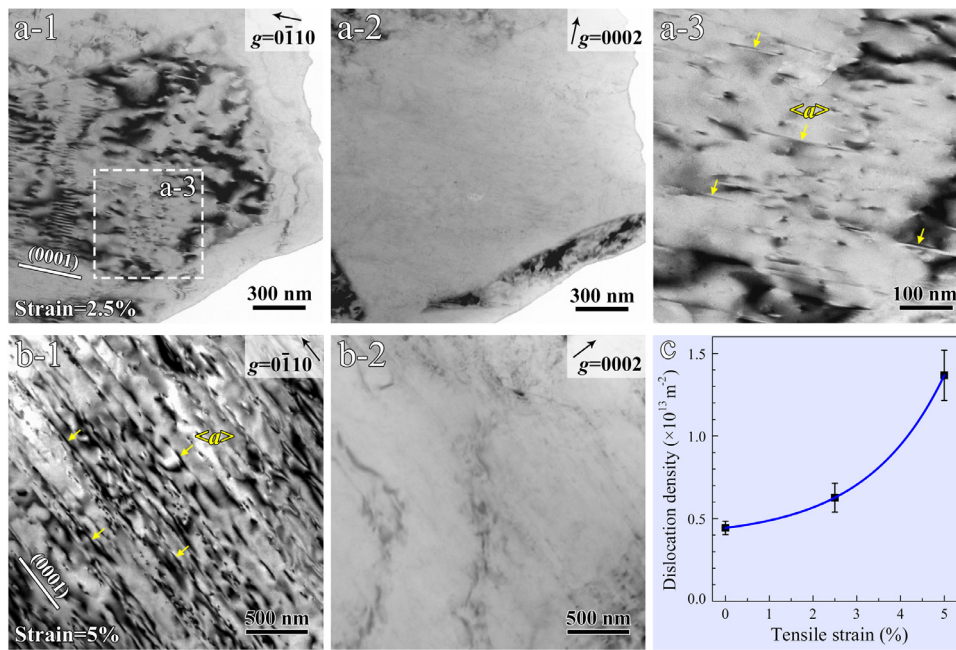
Fig. 6. Dislocation configurations in tensile-deformed coarse-grained pure Mg ($\bar{d}$=125 μm): (a-1) and (a-2) TEM images of 2.5% deformed sample viewed with $g = 0\bar{1}10$ and $g = 0002$, respectively, (a-3) enlarged image of (a-1), (b-1) and (b-2) TEM images of 5% deformed sample viewed with $g = 0\bar{1}10$ and $g = 0002$, respectively, (c) increasing of statistic dislocation density during tensile testing.
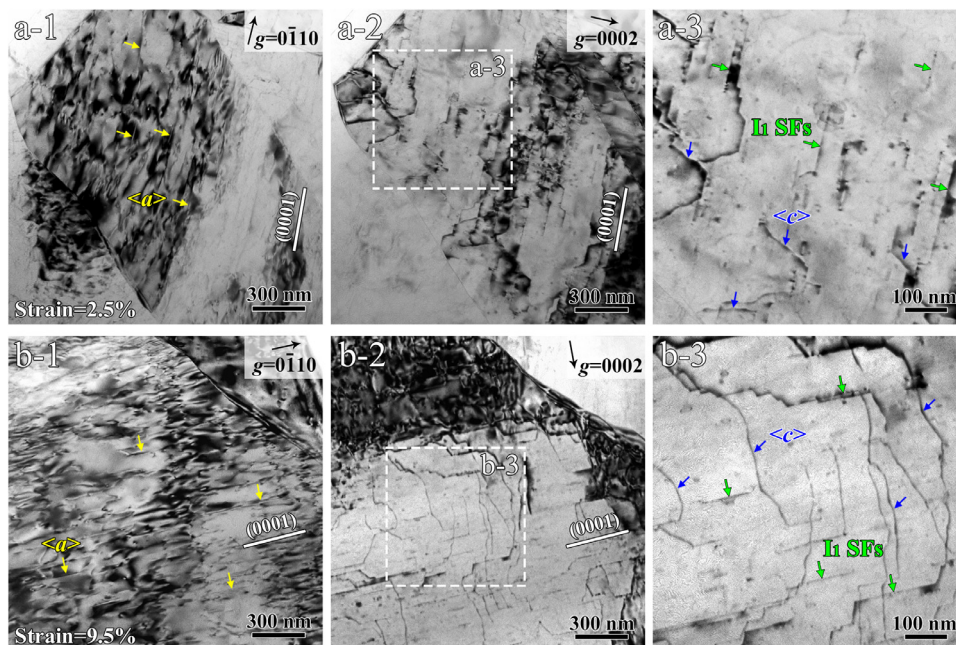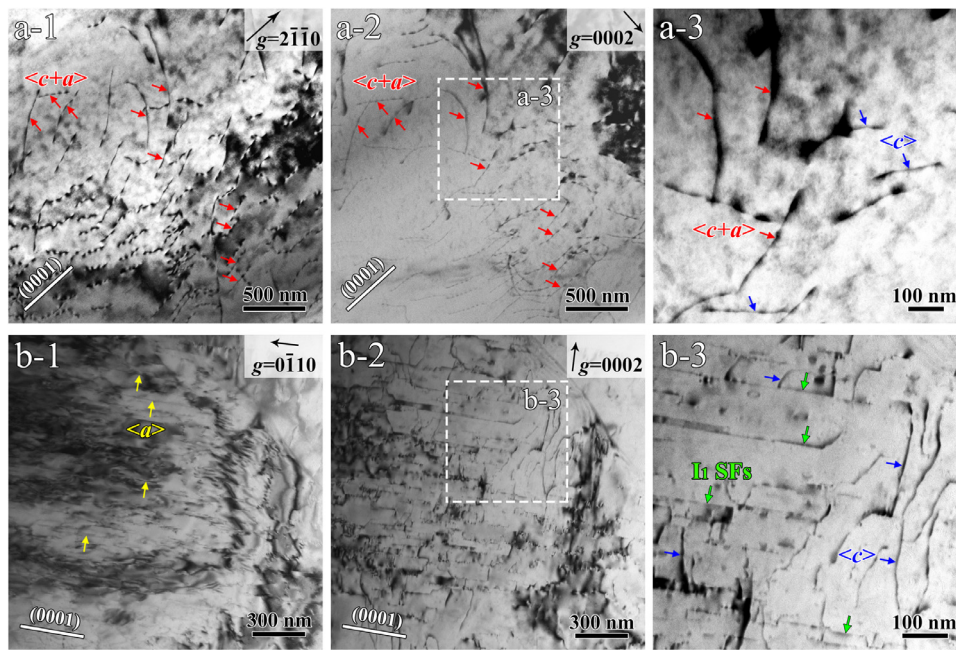

Fig. 7. Dislocation configurations of tensile deformed medium-grained pure Mg ($\bar{d}$=51 μm): (a-1) and (a-2) TEM images of 2.5% deformed sample viewed with $g = 0\bar{1}10$ and $g = 0002$, respectively, (a-3) enlarged image of (a-2), (b-1) and (b-2) TEM images of 9.5% deformed sample viewed with $g = 0\bar{1}10$ and $g = 0002$, respectively, (b-3) enlarged image of (b-2).

a large number of non-basal $\langle c \rangle$ dislocations (marked by the blue arrows) are found in TEM images viewed from the direction of $\mathbf{g} = 0002$ (Fig. 7a-2 and b-2). Previous researches have revealed that $\langle c + a \rangle$ dislocations are easy to be dissociated into $\langle a \rangle$ and $\langle c \rangle$ dislocations [54]. Thus, the accumulated $\langle c \rangle$ dislocations are probably decomposed from pyramidal $\langle c + a \rangle$ dislocations (Fig. 7a-3 and b-3). Additionally, a large number of nano stacking faults (marked by the green arrows) are also observed in the direction of $\mathbf{g} = 0002$ (Fig. 7a-2 and b-2). Most of the stacking faults viewed from this direction are I1 stacking faults, because the Burgers vector of Shock-

ley partial bounding the I2 faults is 1/3 $<0\bar{1}10>$, which is invisible when $\mathbf{g} = 0002$. Moreover, it has been established that the reciprocal of average spacing of stacking faults, 1/d, reveals a linear relationship with yield strength in Mg alloys [50]. As shown in Fig. 7a-3 and b-3, the average spacing of I1 stacking faults in the 2.5% and 9.5% deformed samples are, respectively, ~70 nm and ~45 nm. The nano stacking faults provide additional strengthening in the medium-grained pure Mg.

Fig. 8 shows dislocation configurations in the fine-grained Mg ($\bar{d}$=5.5 μm) subjected to 2.5% strain. Besides basal $\langle a \rangle$ and

Fig. 8. Dislocation configurations of tensile deformed fine-grained pure Mg ($\bar{d}$=5.5 μm): (a-1) and (a-2) TEM images of 2.5% deformed sample viewed with $g = 2\bar{1}\bar{1}0$ and $g = 0002$, respectively, (a-3) enlarged image of (a-2), (b-1) and (b-2) TEM images of 2.5% deformed sample in another position viewed with $g = 0\bar{1}10$ and $g = 0002$, respectively, (b-3) enlarged image of (b-2).

non-basal $\langle c \rangle$ dislocations, numerous $\langle c + a \rangle$ dislocations with Burgers vector of $\boldsymbol{b}=\langle 11\bar{2}3 \rangle$ are found in the grain interior. As shown in Fig. 8a-1 to a-3, the $\langle c + a \rangle$ dislocations (marked by red arrows) are visible in both two-beam conditions of $\boldsymbol{g} = 2\bar{1}\bar{1}0$ and $\boldsymbol{g} = 0002$. The $\langle c + a \rangle$ dislocations were observed glissile in pure Mg micro-pillars under in-situ TEM [5]. Cross-slip of $\langle c + a \rangle$ dislocations occurs on pyramidal I and II planes of Mg, contributing to strain accommodation in the c-axis direction [55]. These observations indicate that $\langle c \rangle$ and $\langle c + a \rangle$ dislocations were activated in fine grains of pure Mg, which notably improved its ductility.

Compared with the medium-grained Mg, the density of stacking faults in fine-grained samples is much higher, as shown in Fig. 8b-1 to b-3. The average spacing of I1 stacking faults in 2.5% deformed sample is ~33 nm. Grain refinement can introduce not only more grain boundaries but also higher density of stacking faults to block dislocation slip. The precise atomic-scale structure of stacking faults and their effects on the mechanical properties will be discussed further in Section 4.1.

4. Discussion

TEM observations indicate that only basal slip systems are activated in the coarse-grained sample (Fig. 6), leading to a poor uniform elongation (UE) of 5.3% (Fig. 3a). Basal slip systems in Mg can only provide two independent slip systems, which is insufficient for uniform deformation of polycrystalline materials according to the Von Mises criterion [3,53]. As the grain size is decreased to 51 μm and 5.5 μm, non-basal slip systems are increasingly activated, which improves the UE to 10.5% and 18.3%, respectively.

4.1. Contributions of nano stacking faults on strengthening and ductilization

I1 stacking faults with nano spacing were frequently observed in grain interiors. HRTEM results show that stacking fault ribbons are bounded by two Frank partials with $\boldsymbol{b} = 1/6\langle 2\bar{2}0\bar{3} \rangle$, as shown in Fig. 9a and b. The I1 stacking faults introduce into the HCP crystal a three-atomic layer of face-centered cubic stacking (ABC) as

shown in Fig. 9c, and its orientation relationship with the Mg Matrix is: $(\bar{1}11)_{\text{stacking fault}}//(0001)_{\alpha}$, $(010)_{\text{stacking fault}}//(03\bar{3}4)_{\alpha}$. I1 stacking faults provide limited blocking effect on perfect $\langle a \rangle$ dislocations, when their Frank partial dislocations interact with dislocations slipping in the basal plane. In contrast, when I1 stacking faults interact with non-basal dislocations, i.e. $\langle c + a \rangle$ dislocations with Burgers vector of $\boldsymbol{b} = 1/3\langle 11\bar{2}3 \rangle$, a strong blocking effect will be provided on dislocation slipping. As shown in Fig. 9d, the slip planes in HCP and FCC are $(11\bar{2}2)$ and (111), respectively. Stacking faults are effective barrier for $\langle c + a \rangle$ dislocations, resulting in significant pinning effects. Fig. 9d shows that the angle between slip planes in HCP and FCC is θ. The driving stress to dislocations in FCC layer is $\tau_{\text{FCC}}=\tau_{\text{HCP}} \times \cos(\pi-\theta)$, which is reduced to ~86% of the original one.

Contribution of stacking faults to increasing of yield strength was raised by Jian et al. [48]. They proposed that the relationship of yield strength is inversely proportional to the average spacing of stacking faults. According to Hall-Petch equation, it has been well established that yield strength improved by grain refinement is inversely proportional to the square root of grain size [49,56]. Consequently, stacking faults are also effective in strengthening, similar to grain boundaries. However, it is difficult to obtain uniform nano spacing stacking faults in most Mg alloys. Peng et al. [57] raised that the volume fraction of stacking faults should be considered when evaluating the strengthening effect, and developed an equation as:

$$\Delta\sigma = \text{mkd}^{-1} \tag{3}$$

where m is the volume fraction of stacking faults, and k is a constant.

From the above analysis, for pure magnesium, the application of this equation can be used only in a grain size range in which $\langle c \rangle$ and/or $\langle c + a \rangle$ dislocations are active. Typical dislocations in coarse grained sample are mainly $\langle a \rangle$ dislocations, which can only slip in basal planes. In this scenario, stacking faults provide little blocking effect, and its strengthening effect cannot be calculated by this equation. When the grain size is reduced to less than 50 μm,
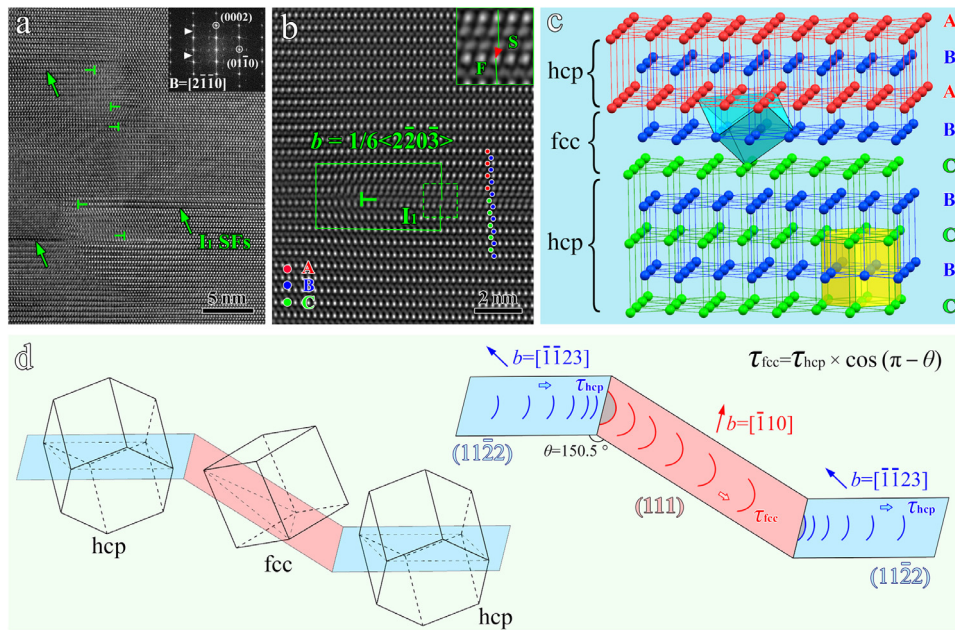
Fig. 9. Atomic scale structure of nano stacking faults in deformed Mg. (a) and (b) HRTEM images of I1 stacking faults in [2$\bar{1}$$\bar{1}$0] zone axis, (c) 3D atomic model of I1 stacking fault, (d) schematic diagram of slip planes near the interfaces of I1 stacking fault.

a large number of non-basal dislocations are activated, leading to a substantial strain hardening.

In addition, the width of stacking faults is considered as another factor for strengthening, because non-basal slip will have a higher chance to be blocked by wider stacking faults. It has been well established that the width of stacking faults is inversely proportional to the stacking fault energy [58]. Fig. 10a shows a typical isolated stacking fault in a fine-grained sample, which has a width of ~42 nm. Geometric phase analysis mapping shows that a pair of mirror symmetrical local strain region exist at the cores of partial dislocation (Fig. 10b). The Burgers circuits S_1F_1 and S_2F_2 (marked in green lines) in Fig. 10c and d indicate that the Burgers vectors of the bounding partial dislocations are 1/6<2$\bar{2}$0$\bar{3}$> and 1/6<$\bar{2}$$\bar{2}$03>, respectively. The opposite Burgers vectors result in no closure failure in the larger Burgers circuit S_0F_0 in Fig. 10a.

On the other hand, I1 stacking faults also exhibit significant contribution for inducing non-basal slip, which is very important for ductilization of Mg alloys. Fig. 11a-1 shows a high resolution TEM image of a basal ⟨a⟩ dislocation, which has a Burgers vector of $\boldsymbol{b}$ = 1/3<11$\bar{2}$0>. Based on the HRTEM image, GPA is carried out around the dislocation cores. As shown in Fig. 11a-2, little local strain is induced by perfect ⟨a⟩ dislocation in the normal direction of (0001) plane. In contrast, Frank partial dislocation induces a much larger local strain in this direction (Fig. 11b-1 and b-2). Quantitative linear analysis of local strain reveals that Frank partial dislocations induces ~4% of tensile strain and ~6% of compressive strain at dislocation cores (Fig. 11c). Consequently, the c/a ratio of Mg matrix is decreased in some local areas. Bu et al. reported that the c/a ratio is closely related to the structural plane features that govern activation of slip systems in hcp metals. Reduction of c/a ratio significantly promotes ⟨c + a⟩ slip in HCP structural materials [59]. As shown in Fig. 11d, the regions of negative strain of Frank partial dislocations have a much lower c/a ratio to less than 1.55, which are the potential dislocation sources of non-basal slips. Thus, I1 faults acted as heterogeneous nucleation sources for perfect ⟨c + a⟩ dislocations, and thus significantly enhancing ductility of Mg alloys [12,58]. This source mechanism was also energetically feasible for extensive fault geometries proposed by Agnew et al. [60].

4.2. Formation mechanisms of ⟨c⟩ dislocations

As mentioned above, non-basal dislocations in pure Mg are activated with decreasing grain size. When the grain size is reduced to less than 5 μm, a large number of ⟨c + a⟩ dislocations are formed, leading to significant increase in ductility. Note that we found high density of ⟨c⟩ dislocations and I1 stacking faults before the formation of ⟨c + a⟩ dislocations in the medium-grained sample (Fig. 7). This raises a question on if the ⟨c⟩ and ⟨c + a⟩ dislocations are correlated.

As shown in Fig. 12a and b, some typical ⟨c⟩ dislocations are marked by blue arrows in bright-field and dark field TEM images, viewed from the direction of $\boldsymbol{g}$ = 0002. We hypothesize that the formation of ⟨c⟩ dislocations could be formed by the dissociation of ⟨c + a⟩ dislocations. Fig. 12c schematically illustrates the details of this process. In stage I, a pure ⟨c + a⟩ dislocation is slipping in the pyramidal plane towards right. Due to the relatively low flow stress in the medium-grained samples, the slip basal ⟨a⟩ dislocation, which is easier to activated, is still dominant. The ⟨c + a⟩ dislocation becomes sessile when it moves to intersection region of pyramidal and adjacent planes. In order to reduce the energy [54], the dislocation dissociates into ⟨c⟩ and ⟨a⟩ dislocations (Stage II). The ⟨a⟩ dislocation is glissile away, leaving behind the sessile ⟨c⟩ dislocation (Stage III). This dissociation process can thus be expressed in Eq. (4).

$$1/3\langle 11\bar{2}3\rangle \rightarrow \langle 0001\rangle + 1/3\langle 11\bar{2}0\rangle \qquad (4)$$

In the medium and fine-grained samples, another typical scenario is frequently observed, in which the tips of ⟨c⟩ dislocations and I1 stacking faults are connected Fig. 13a and b). This microstructural morphology looks like a ⟨c⟩ dislocation blocked by an I1 stacking fault. It has been well established that both the ⟨c⟩ dislocations and I1 stacking faults in HCP structural materials are sessile [61]. Hence, it is more reasonable to consider the formation mechanism of this structure formed by growth or dissociation. Fig. 13c shows a schematic diagram of a proposed formation mechanism. A ⟨c + a⟩ dislocation is slipping in the pyramidal plane towards right. The ⟨c + a⟩ dislocation is not stable, and tend to dissociate, forming a ribbon of I1 fault [13,62]. As mentioned in
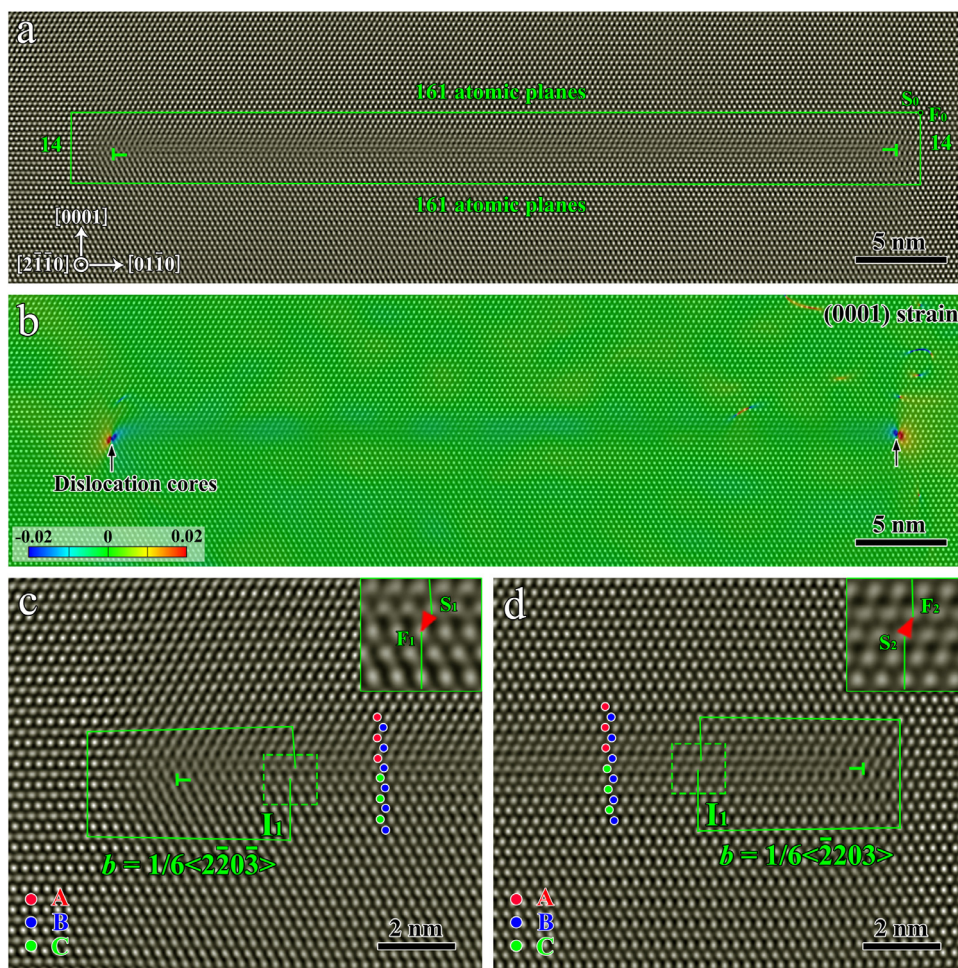
Fig. 10. Atomic-scale microstructure of a typical isolated stacking fault in a fine-grained sample. (a) HRTEM image, (b) GPA mapping overlapped with the HRTEM image, (c) and (d) enlarged images of left and right sides of this fault.
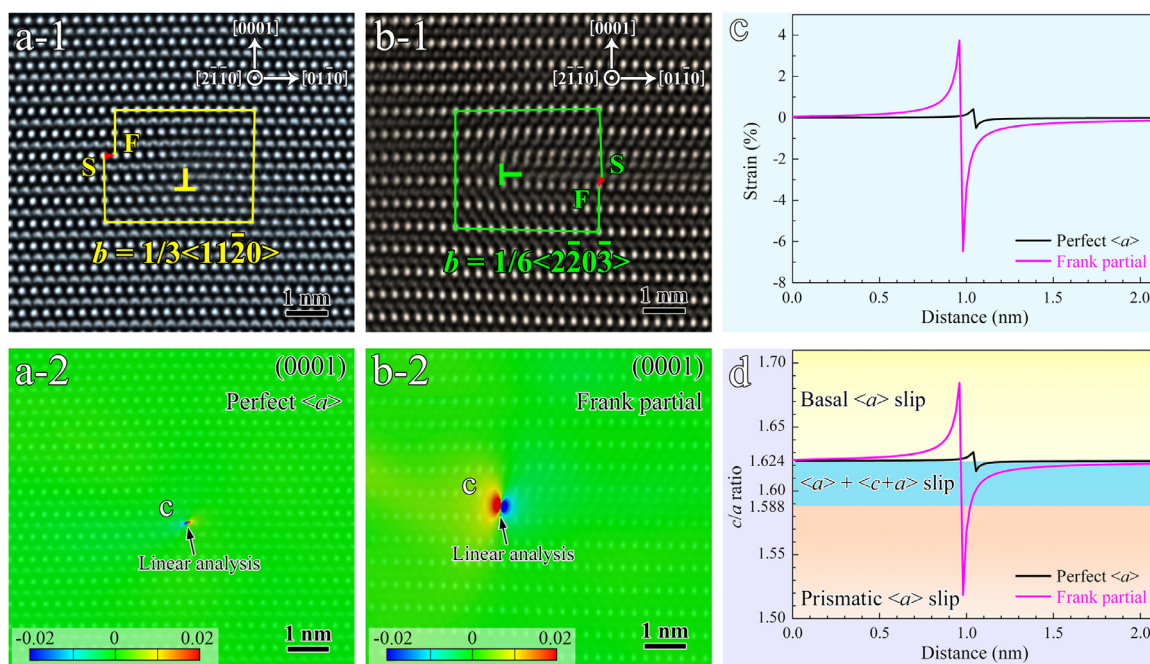
Fig. 11. Atomic structure of dislocation cores. (a-1) and (a-2) HRTEM image and GPA mapping of perfect ⟨a⟩ dislocation, (b-1) and (b-2) HRTEM image and GPA mapping of Frank partial dislocation, (c) Linear analysis of local strain at dislocation core, (d) Distribution of c/a ratio around dislocation cores, in which three distinct regimes are indicated according to the activated crystallographic deformation modes [59].
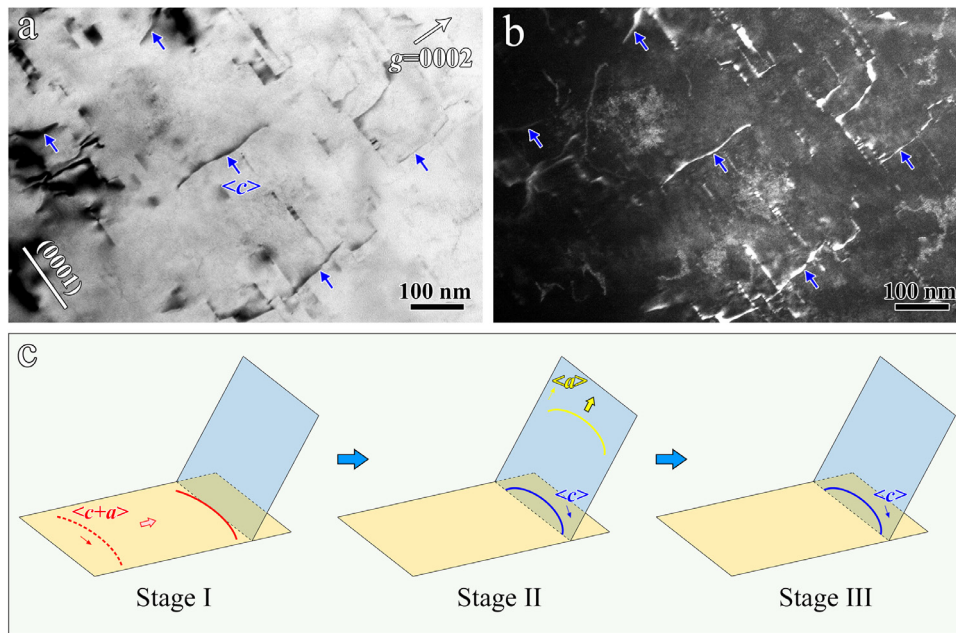
Fig. 12. Formation mechanism of ⟨c⟩ dislocations in pure Mg. (a) and (b) bright field and weak beam dark field TEM images, viewed from the direction of g = 0002, (c) schematic diagram of process of dislocation dissociation.
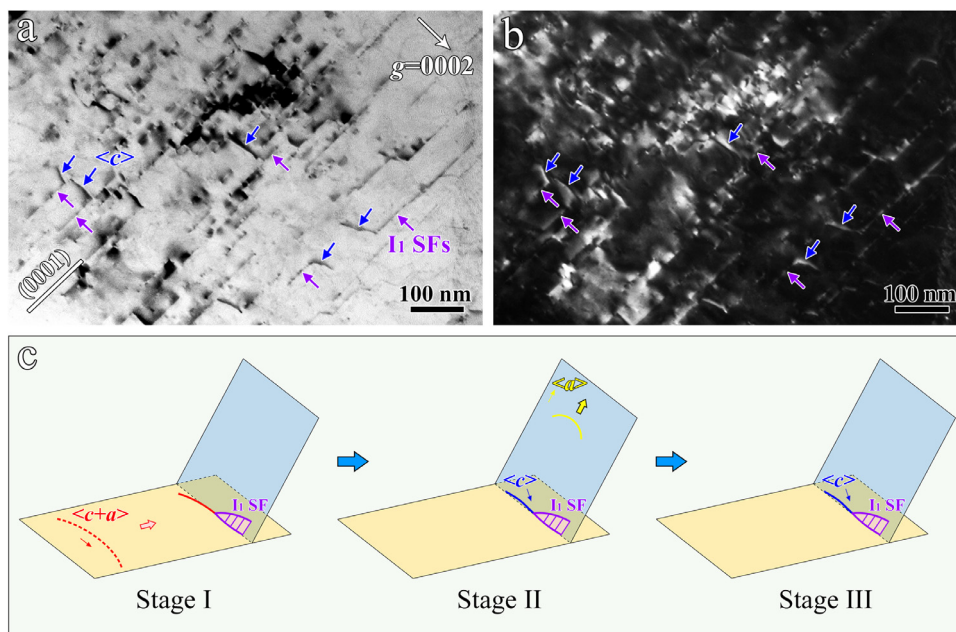
Fig. 13. Formation mechanism of connected ⟨c⟩ dislocations and stacking faults in pure Mg. (a) and (b) bright field and weak beam dark field TEM images, viewing from the direction of g = 0002, (c) schematic diagram of the process of dislocation dissociation.

Fig. 10, the width of a stacking fault is inversely proportional to the stacking fault energy. In local regions, segments of the perfect ⟨c + a⟩ dislocation could be separated to leading and trailing partials, providing the temporary pinning of the ⟨c + a⟩ dislocation (Stage I). Meanwhile, the rest part of the ⟨c + a⟩ dislocation dissociated in another way, forming a sessile ⟨c⟩ and a glissile ⟨a⟩ dislocation (Stage II). It has been discussed that stacking faults provide little blocking effect on perfect ⟨a⟩ dislocation. The ⟨a⟩ dislocation slips away, leaving the ⟨c⟩ dislocation connects with the I1 fault (Stage III). The dissociation process of this part can be presented in Eqs. (4) and ((5):

$$1/3\langle11\bar{2}3\rangle \rightarrow 1/6\langle20\bar{2}3\rangle + 1/6\langle02\bar{2}3\rangle \tag{5}$$

5. Conclusions

In summary, non-basal dislocations are activated in the pure Mg samples with decreasing grain size from 125 μm to 51 and 5.5 μm, which leads to simultaneous increase in strength and ductility. The key findings are summarized as follows:

(1) In coarse grained samples ($\bar{d}$=125 μm) only basal ⟨a⟩ dislocations are activated. As the grain size is reduced to 51 μm, additional ⟨c⟩ dislocations and I1 stacking faults are formed, co-exiting with ⟨a⟩ dislocations. Further reduction of grain size to 5.5 μm activated ⟨c + a⟩ dislocations. The activation of non-basal dislocations helps to accommodate strain along c-axis and improves the uniform elongation of pure Mg from 5.3% to 10.5% to 18.3%.

(2) In addition to the conventional strengthening by grain refinement, high density of nano-spaced stacking faults acted as another strengthening mechanism, cooperating. The strengthening induced by stacking faults in pure Mg only occurred when grain sizes are reduced below 50 μm.

(3) The flow stress is increased with decreasing grain size, leading to activation of $\langle c + a \rangle$ dislocations. However, the $\langle c + a \rangle$ dislocations are unstable, which are dissociated in two ways: $\langle c \rangle$ and $\langle a \rangle$ dislocations, or into I1 stacking faults.

Declaration of Competing Interest

The authors declare that they have no known competing financial interests or personal relationships that could have appeared to influence the work reported in this paper.

Acknowledgments

References

[1] T.M. Pollock, Weight loss with magnesium alloys, Science 328 (2010) 986–987.

[2] J.F. Nie, Effects of precipitate shape and orientation on dispersion strengthening in magnesium alloys, Scripta Mater. 48 (2003) 1009–1015.

[3] W.B. Hutchinson, M.R. Barnett, Effective values of critical resolved shear stress for slip in polycrystalline magnesium and other hcp metals, Scripta Mater. 63 (2010) 737–740.

[4] Z.X. Wu, W.A. Curtin, Mechanism and energetics of <c+a>dislocation cross-slip in hcp metals, Proc. Natl. Acad. Sci. USA 113 (2016) 11137–11142.

[5] B.Y. Liu, F. Liu, N. Yang, X.B. Zhai, L. Zhang, Y. Yang, B. Li, J. Li, E. Ma, J.F. Nie, Z.W. Shan, Large plasticity in magnesium mediated by pyramidal dislocations, Science 365 (2019) 73–75.

[6] O. Orlov, G. Raab, T.T. Lamark, M. Popov, Y. Estrin, Improvement of mechanical properties of magnesium alloy ZK60 by integrated extrusion and equal channel angular pressing, Acta Mater. 59 (2011) 375–385.

[7] R.B. Figueiredo, T.G. Langdon, Strategies for achieving high strain rate superplasticity in magnesium alloys processed by equal-channel angular pressing, Scripta Mater. 61 (2009) 84–87.

[8] K. Máthis, K. Nyilasa, A. Axt, I. Dragomir-Cernatescu, T. Ungár, P. Lukáč, The evolution of non-basal dislocations as a function of deformation temperature in pure magnesium determined by X-ray diffraction, Acta Mater. 52 (2004) 2889–2894.

[9] H. Zhou, H.Y. Ning, X.L. Ma, D.D. Yin, L.R. Xiao, X.C. Sha, Y.D. Yu, Q.D. Wang, Y.S. Li, Microstructural evolution and mechanical properties of Mg-9.8Gd-2.7Y-0.4Zr alloy produced by repetitive upsetting, J. Mater. Sci. Technol. 34 (2018) 1067–1075.

[10] H. Zhou, Q.D. Wang, W. Guo, B. Ye, W.W. Jian, W.Z. Xu, X.L. Ma, J. Moering, Finite element simulation and experimental investigation on homogeneity of Mg-9.8Gd-2.7Y-0.4Zr magnesium alloy processed by repeated-upsetting, J. Mater. Process. Tech. 225 (2015) 310–317.

[11] H. Sun, Z.G. Ding, D.L. Zhang, H. Zhou, S. Li, E.J. Lavernia, Y.T. Zhu, W. Liu, Predicting the formation of <c+a>dislocations in magnesium alloys from multiple stacking fault energies, Materialia 7 (2019) 100352.

[12] S. Sandlöbes, Z. Pei, M. Friák, L.F. Zhu, F. Wang, S. Zaefferer, D. Raabe, J. Neugebauer, Ductility improvement of Mg alloys by solid solution: ab initio modeling, synthesis and mechanical properties, Acta Mater. 70 (2014) 92–104.

[13] Z.X. Wu, R. Ahmad, B.L. Yin, S. Sandlöbes, W.A. Curtin, Mechanistic origin and prediction of enhanced ductility in magnesium alloys, Science 359 (2018) 447–452.

[14] K. Wei, L.R. Xiao, B. Gao, L. Li, Y. Liu, Z.G. Ding, W. Liu, H. Zhou, Y.H. Zhao, Enhancing the strain hardening and ductility of Mg-Y alloy by introducing stacking faults, J. Magn. Alloys 8 (2020) 1221–1227.

[15] G.M. Zhu, L.Y. Wang, H. Zhou, J.H. Wang, Y. Shen, P. Tu, H. Zhu, W. Liu, P.P. Jin, X.Q. Zeng, Improving ductility of a Mg alloy via non-basal <a>slip induced by Ca addition, Int. J. Plast. 120 (2019) 164–179.

[16] J. Zhang, Y.C. Dou, G.B. Liu, Z.X. Guo, First-principles study of stacking fault energies in Mg-based binary alloys, Comput. Mater. Sci. 79 (2013) 564–569.

[17] Y.F. Wu, S. Li, Z.G. Ding, W. Liu, Y.H. Zhao, Y.T. Zhu, Effect of charge redistribution factor on stacking-fault energies of Mg-based binary alloys, Scripta Mater 112 (2016) 101–105.

[18] X.L. Wu, Y.T. Zhu, Inverse grain-size effect on twinning in nanocrystalline Ni, Phys. Rev. Lett. 101 (2008) 025503.

[19] X.L. Ma, W.Z. Xu, H. Zhou, J.A. Moering, J. Narayan, Y.T. Zhu, Alloying effect on grain-size dependent deformation twinning in nanocrystalline Cu–Zn alloys, Philos. Mag. 95 (2015) 301–310.

[20] Y.T. Zhu, X.Z. Liao, X.L. Wu, Deformation twinning in nanocrystallne materials, Prog. Mater. Sci. 57 (2012) 1–62.

[21] G.M. Cheng, W.W. Jian, W.Z. Xu, H. Yuan, P.C. Millett, Y.T. Zhu, Grain size effect on deformation mechanisms of nanocrystalline bcc metals, Mater. Res. Lett. 1 (2013) 26–31.

[22] J. Koike, T. Kobayashi, T. Mukai, H. Watanabe, M. Suzuki, K. Maruyama, K. Higashi, The activity of non-basal slip systems and dynamic recovery at room temperature in fine-grained AZ31B magnesium alloys, Acta Mater. 51 (2003) 2055–2065.

[23] X. Luo, Z.Q. Feng, T.B. Yu, J.Q. Luo, T.L. Huang, G.L. Wu, N. Hansen, X.X. Huang, Transitions in mechanical behavior and in deformation mechanisms enhance the strength and ductility of Mg-3Gd, Acta Mater. 183 (2020) 398–407.

[24] J.A. del Valle, F. Carreño, O.A. Ruano, Influence of texture and grain size on work hardening and ductility in magnesium-based alloys processed by ECAP and rolling, Acta Mater. 54 (2006) 4247–4259.

[25] A. Jain, O. Duygulu, D.W. Brown, C.N. Tomé, S.R. Agnew, Grain size effects on the tensile properties and deformation mechanisms of a magnesium, AZ31B, sheet, Mater. Sci. Eng. A 486 (2008) 545–555.

[26] A. Kula, C.J. Silva, M. Niewczas, Grain size effect on deformation behaviour of Mg-Sc alloys, J. Alloys Comp. 727 (2017) 642–657.

[27] H.D. Fan, S. Aubry, A. Arsenlis, J.A. El-Awady, Grain size effects on dislocation and twinning mediated plasticity in magnesium, Scripta Mater. 112 (2016) 50–53.

[28] Z.R. Zeng, J.F. Nie, S.W. Xu, C.H.J. Davies, N. Birbilis, Super-formable pure magnesium at room temperature, Nat. Commun. 8 (2017) 972.

[29] H. Somekawa, T. Mukai, Hall-Petch breakdown in fine-grained pure magnesium at low strain rates, Metall. Mater. Trans. A 46 (2015) 894–902.

[30] R.B. Figueiredo, F.S.J. Poggiali, C.L.P. Silva, P.R. Cetlin, T.G. Langdon, The influence of grain size and strain rate on the mechanical behavior of pure magnesium, J. Mater. Sci. 51 (2016) 3013–3024.

[31] R.B. Figueiredo, S. Sabbaghianrad, A. Giwa, J.R. Greer, T.G. Langdon, Evidence for exceptional low temperature ductility in polycrystalline magnesium processed by severe plastic deformation, Acta Mater. 122 (2017) 322–331.

[32] X.L. Ma, C.X. Huang, W.Z. Xu, H. Zhou, X.L. Wu, Y.T. Zhu, Strain hardening and ductility in a coarse-grain/nanostructure laminate material, Scripta Mater. 103 (2015) 57–60.

[33] L.R. Xiao, X.F. Chen, K. Wei, Y. Liu, D.D. Yin, Z.H. Hu, H. Zhou, Y.T. Zhu, Effect of dislocation configuration on Ag segregation in subgrain boundary of a Mg-Ag alloy, Scripta Mater 191 (2021) 219–224.

[34] C.M. Cepeda-Jiménez, J.M. Molina-Aldareguia, M.T. Pérez-Prado, Effect of grain size on slip activity in pure magnesium polycrystals, Acta Mater. 84 (2015) 443–456.

[35] C.M. Cepeda-Jiménez, J.M. Molina-Aldareguia, M.T. Pérez-Prado, Origin of the twinning to slip transition with grain size refinement, with decreasing strain rate and with increasing temperature in magnesium, Acta Mater. 88 (2015) 232–244.

[36] Y. Wang, H. Choo, Influence of texture on Hall-Petch relationships in an Mg alloy, Acta Mater 81 (2014) 83–97.

[37] B. Guan, Y.C. Xin, X.X. Huang, P.D. Wu, Q. Liu, Quantitative prediction of texture effect on Hall-Petch slope for magnesium alloys, Acta Mater. 173 (2019) 142–152.

[38] D.D. Yin, C.J. Boehlert, L.J. Long, G.H. Huang, H. Zhou, J. Zheng, Q.D. Wang, Tension-compression asymmetry and the underlying slip/twinning activity in extruded Mg-Y sheets, Int. J. Plast. 136 (2021) 102878.

[39] T.H. Courney, in: Mechanical Behavior of Materials, 2nd ed., McGraw-Hill, 2000, p. 13.

[40] E.W. Hart, Theory of the tensile test, Acta Metall. 15 (1967) 351–355.

[41] R.X. Zheng, J.P. Du, S. Gao, H. Somekawa, S. Ogata, N. Tsuji, Transition of dominant deformation mode in bulk polycrystalline pure Mg by ultra-grain refinement down to sub-micrometer, Acta Mater. 198 (2020) 35–46.

[42] O. Bouaziz, S. Allain, C.P. Scott, P. Cugy, D. Barbier, High manganese austenitic twinning induced plasticity steels: a review of the microstructure properties relationships, Curr. Opin. Solid State Mater. Sci. 15 (2011) 141–168.

[43] X.L. Wu, P. Jiang, L. Chen, F.P. Yuan, Y.T. Zhu, Extraordinary strain hardening by gradient structure, Proc. Natl. Acad. Sci. USA 111 (2014) 7197–7201.

[44] J.C. Tan, M.J. Tan, Dynamic continuous recrystallization characteristics in two stage deformation of Mg–3Al–1 Zn alloy sheet, Mater. Sci. Eng. A 339 (2003) 124–132.

[45] D.W. Brown, S.R. Agnew, M.A.M. Bourke, T.M. Holden, S.C. Vogel, C.N. Tomé, Internal strain and texture evolution during deformation twinning in magnesium, Mater. Sci. Eng. A 399 (2005) 1–12.

[46] J. Wang, J.P. Hirth, C.N. Tomé, Twinning nucleation mechanisms in hexagonal–close-packed crystals, Acta Mater. 57 (2009) 5521–5530.

[47] Q. Yu, L. Qi, K. Chen, R.K. Mishra, J. Li, A.M. Minor, The nanostructured origin of deformation twinning, Nano Lett. 12 (2012) 887–892.

[48] W.W. Jian, G.M. Cheng, W.Z. Xu, H. Yuan, M.H. Tsai, Q.D. Wang, C.C. Koch, Y.T. Zhu, S.N. Mathaudhu, Ultrastrong Mg alloy via nano-spaced stacking faults, Mater. Res. Lett. 1 (2013) 61–66.

[49] N.J. Petch, The cleavage strength of polycrystals, J. Iron. Steel. Inst. 174 (1953) 25–28.

[50] W.W. Jian, G.M. Cheng, W.Z. Xu, C.C. Koch, Q.D. Wang, Y.T. Zhu, S.N. Mathaudhu, Physics and model of strengthening by parallel stacking faults, App. Phys. Lett. 103 (2013) 133108.

[51] D.L. Zhang, H.M. Wen, M.A. Kumar, F. Chen, L.M. Zhang, I.J. Beyerlein, J.M. Schoenung, S. Mahajan, E.J. Lavernia, Yield symmetry and reduced strength differential in Mg-2.5Y alloy, Acta Mater. 120 (2016) 75–85.

[52] N. Dixit, K.Y. Xie, K.J. Hemker, K.T. Ramesh, Microstructural evolution of pure magnesium under high strain rate loading, Acta Mater. 87 (2015) 56–67.

[53] U.M. Chaudry, K. Hamad, J.-.G. Kim, On the ductility of magnesium based materials: a mini review, J. Alloys Comp. 792 (2019) 652–664.

[54] D.L. Zhang, L. Jiang, J.M. Schoenung, S. Mahajan, E.J. Lavernia, TEM study on relationship between stacking faults and non-basal dislocations in Mg, Philos. Mag. 95 (2015) 3823–3844.

[55] Y.Z. Tang, J.A. El-Awady, Formation and slip of pyramidal dislocations in hexagonal close-packed magnesium single crystals, Acta Mater. 71 (2014) 319–332.

[56] B. Gao, Q.Q. Lai, Y. Cao, R. Hu, L.R. Xiao, Z.Y. Pan, N.N. Liang, Y.S. Li, G. Sha, M.P. Liu, H. Zhou, X.L. Wu, Y.T. Zhu, Ultrastrong low-carbon nanosteel produced by heterostructure and interstitial mediated warm rolling, Sci. Adv. 6 (2020) eaba8169.

[57] Q.M. Peng, Y. Sun, B.C. Ge, H. Fu, Q. Zu, X.Z. Tang, J.Y. Huang, Interactive contraction nanotwins-stacking faults strengthening mechanism of Mg alloys, Acta Mater. 169 (2019) 36–44.

[58] S. Sandlöbes, M. Friák, S. Zaefferer, A. Dick, S. Yi, D. Letzig, Z. Pei, L.F. Zhu, J. Neugebauer, D. Raabe, The relation between ductility and stacking fault energies in Mg and Mg-Y alloys, Acta Mater 60 (2012) 3011–3021.

[59] Y.Q. Bu, Z.M. Li, J.B. Liu, H.T. Wang, D. Raabe, W. Yang, Nonbasal slip systems enable a strong and ductile hexagonal-close-packed high-entropy phase, Phys. Rev. Lett. 122 (2019) 075502.

[60] S.R. Agnew, L. Capolungo, C.A. Calhoun, Connections between the basal I1 "growth" fault and <c+a>dislocations, Acta Mater 82 (2015) 255–265.

[61] Z.X. Wu, W.A. Curtin, The origins of high hardening and low ductility in magnesium, Nature 526 (2015) 62–67.

[62] J. Geng, M.F. Chisholm, R.K. Mishra, K.S. Kumar, The structure of <c+a>type dislocation loops in magnesium, Philos. Mag. Lett. 94 (2014) 377–386.